Dark-matter decays and self-gravitating halos

Annika H. G. Peter*

California Institute of Technology, Mail Code 249-17, Pasadena, California 91125, USA

Christopher E. Moody

Department of Physics, University of California, Santa Cruz, California 95064, USA

Marc Kamionkowski

California Institute of Technology, Mail Code 350-17, Pasadena, California 91125, USA

We consider models in which a dark-matter particle decays to a slightly less massive daughter particle and a noninteracting massless particle. The decay gives the daughter particle a small velocity kick. Self-gravitating dark-matter halos that have a virial velocity smaller than this velocity kick may be disrupted by these particle decays, while those with larger virial velocities will be heated. We use numerical simulations to follow the detailed evolution of the total mass and density profile of self-gravitating systems composed of particles that undergo such velocity kicks as a function of the kick speed (relative to the virial velocity) and the decay time (relative to the dynamical time). We show how these decays will affect the halo mass-concentration relation and mass function. Using measurements of the halo mass-concentration relation and galaxy-cluster mass function to constrain the lifetime–kick-velocity parameter space for decaying dark matter, we find roughly that the observations rule out the combination of kick velocities greater than 100 km s^{-1} and decay times less than a few times the age of the Universe.

I. INTRODUCTION

There is a good consensus from many types of observations that dark matter makes up ~25% of the mass-energy density of the Universe [1–5]. However, the nature of dark matter is unknown. The most popular class of candidates is the weakly interacting massive particle (WIMP), since such particles may be produced thermally in the early Universe at the right abundance and with behavior consistent with a large set of cosmological observations [6–10]. The canonical WIMP is electrically neutral, and it is stable. Once produced in the early Universe, it interacts with itself and with ordinary matter only gravitationally. If the WIMP is the dark matter, then the dark halos of galaxies and galaxy clusters are described by a collisionless gas of self-gravitating WIMPs.

However, there is both theoretical and observational room for other types of dark-matter candidates. While observations are *consistent* with WIMPs, the observations do not *require* the dark matter to be WIMPs. Moreover, some observations—e.g., of the inner mass distribution in galaxies and/or the abundance subhalos in dark-matter halos [11]—have inspired theoretical searches for dark-matter candidates with properties beyond those of the canonical WIMP. There is a large amount of literature on dark-matter particles with additional physical properties beyond those of the canonical stable collisionless WIMP.

Examples include (but are by no means limited to) particles with small electric charges [12] or dipoles [13], self-interacting particles [14], or particles with long-range forces [15–19] (see Refs. [20,21] for recent reviews).

In the spirit of these lines of investigation, we consider in this work a neutral dark-matter particle X of mass M_X that decays with lifetime τ to a slightly less massive neutral particle Y of mass $M_Y = M_X(1 - \epsilon)$ with $\epsilon \ll 1$ and an effectively massless particle ζ which is itself assumed to be noninteracting. We imagine that such a scenario may arise in some implementations of models of inelastic dark matter [22].

When the X particle decays, the daughter Y particle receives a nonrelativistic velocity kick $v_k \simeq \epsilon c$. Now suppose that these particles make up a self-gravitating halo of virial velocity $v_{\rm vir}$. If $v_k \ll v_{\rm vir}$, then the halo may be heated slightly, and its mass distribution thus rearranged slightly, by the velocity kicks imparted to the Y particles once most of the X particles have decayed. If, on the other hand, $v_k \gg v_{\rm vir}$, then these halos will be completely disrupted after most of the X particles have decayed. There should thus be no halos with $v_{\rm vir} \ll v_k$ if these particles decay with lifetimes τ small compared with the age $t_{\rm H}$ of the Universe, and this has been postulated as a possible explanation for the low number of dwarf galaxies relative to that expected from dissipationless dark-matter simulations [23,24]. Alternatively, if $v_k \gg v_{\rm vir}$ but $\tau \gg t_{\rm H}$, then only a small fraction ($\sim \tau/t_{\rm H}$) of the halo particles will be kicked out of the halo. The resulting halo mass and mass

*apeter@astro.caltech.edu

distribution may then be affected slightly without being completely disrupted. The canonical-WIMP halo is, of course, recovered in the limits $\tau \rightarrow \infty$ and/or $\epsilon \rightarrow 0$.

In this paper, we report on simulations of self-gravitating halos with decaying particles. While the results of these decays can be understood in the limits $\tau \gtrsim t_H$ and $v_k \gg v_{\rm vir}$ [25] using the adiabatic-expansion model [26,27], detailed evolution of the halo over the full range of the τ-v_k parameter space requires numerical simulation. We use the simulations and observations of the galaxy-cluster mass function and the halo mass-concentration relation to constrain the decay parameter space. Our central results are presented in Fig. 8, which shows that (roughly) the combination of decay times less than a few times the age of the Universe and kick velocities greater than $100 \, \rm km \, s^{-1}$ are ruled out.

The outline of the paper is as follows. In Sec. II, we describe our simulations. In Sec. III, we characterize the evolution of dark-matter halos as a function of the decay parameters using the simulations, and show how the simulations, in conjunction with observational and theoretical (in the context of WIMPs) determinations of the cluster mass function and the mass-concentration relation, allow us to constrain the decay parameter space. In Sec. IV, we discuss various aspects of our findings, including resolution effects (with an eye towards the requirements for cosmological simulations) and observational biases. We summarize our work in Sec. V.

II. SIMULATIONS

We simulate isolated equilibrium dark-matter halos using the parallel N-body code GADGET-2 in its Newtonian, noncosmological mode [28,29]. We have modified GADGET-2 in the following way to handle decays. The maximum time step $\Delta t_{\rm max}$ allowed in the simulations is chosen such that the probability for a decay within that maximum time step is well described by $P_{\rm max} = \Delta t_{\rm max}/\tau \ll 1$. At each time step, there is a Monte Carlo simulation of decays, with the decay probability being $P = \Delta t/\tau$ for each particle. If a particle is designated for decay, it receives a kick speed v_k in a random direction, and is flagged to ensure that the particle cannot decay again. Because we assume the mass difference is negligible throughout the simulations ($\epsilon \lesssim 10^{-3}$), we maintain the mass of the particles; the change in the kinetic energy of the particle due to the kick is much greater than the change to the potential energy due to the decrease in particle mass. The massless ζ particle escapes from the halo and is not of interest in this calculation.

Our halos are spherically symmetric, and the density $\rho(r)$ as a function of galactocentric radius r is taken to be the Navarro-Frenk-White (NFW) form [30,31],

$$\rho(r) = \frac{\rho_s}{(r/r_s)(1 + (r/r_s))^2}, \quad (1)$$

where ρ_s is the scale density, and r_s is the scale radius, such that the halo concentration is

$$c = \frac{R_{\rm vir}}{r_s}, \quad (2)$$

where $R_{\rm vir}$ is the virial radius, or size, of the halo. We define virial quantities with respect to the spherical top-hat overdensity, such that the virial mass

$$M_{\rm vir} = \frac{4\pi}{3} \Delta_v \rho_m R_{\rm vir}^3, \quad (3)$$

where ρ_m is the mean matter density of the Universe, and $\Delta_v = (18\pi^2 + 39x - 82x^2)/\Omega_m(z)$ in a ΛCDM Universe, where $x = \Omega_m(z) - 1$ and Ω_m is the fraction of the critical density ρ_c in the form of matter ($\rho_m = \Omega_m \rho_c$) [32].

The initial velocity distribution must be taken to be consistent with the mass distribution so that the effects of decay are not confused with relaxation of an initially nonequilibrium halo to equilibrium. We take the velocity ellipsoid to be isotropic, a reasonable first approximation to dark-matter halos [33]. This allows us to use Eddington's formula,

$$f(\mathcal{E}) = \frac{1}{\sqrt{8}\pi^2} \left[\int_0^{\mathcal{E}} \frac{d^2\rho}{d\Psi^2} \frac{d\Psi}{\sqrt{\mathcal{E} - \Psi}} + \frac{1}{\sqrt{\mathcal{E}}} \left(\frac{d\rho}{d\Psi} \right)_{\Psi=0} \right], \quad (4)$$

to relate the particle distribution function (DF) $f(\mathcal{E})$ as a function of the negative energy $\mathcal{E}$ ($\mathcal{E} > 0$ for all particles bound to the halo) to known functions, the density and gravitational potential profile Ψ.

We cannot use Eq. (1) in Eq. (4) for arbitrary r; the mass of a halo corresponding to a density profile given by Eq. (4) is formally infinite. Thus, we must truncate the mass profile of the halo, but with care such that the distribution function is everywhere positive-definite. We use the truncation scheme advocated by Kazantzidis et al. (2004) [34],

$$\rho(r) = \begin{cases} \frac{\rho_s}{(r/r_s)(1 + (r/r_s))^2} & r < r_c \\ \frac{\rho_s}{(r/r_s)(1 + (r/r_s))^2} \left(\frac{r}{r_c}\right)^\alpha e^{-(r-r_c)/r_d} & r \geq r_c. \end{cases} \quad (5)$$

The density profile has been exponentially truncated at the cutoff radius r_c and with the parameter r_d controlling the sharpness of the transition. Continuity of the function and its logarithmic slope demands that

$$\alpha = -\frac{1 + 3r_c/r_s}{1 + r_c/r_s} + \frac{r_c}{r_d}. \quad (6)$$

To set the initial positions and velocities of the particles, we sample the DF using an acceptance-rejection method to find the initial radii and speeds [35]. The radius and speed are then isotropically mapped to three spatial coordinates.

A. Parameters

We begin every simulation with identical initial conditions, varying only the concentration c of the NFW profile,

particle lifetimes, and kick velocities. We simulate $M_{\rm vir} = 10^{12} M_\odot$ halos only, but we can extrapolate our results to other halo masses by considering the structural changes to the halos as a function of the decay parameters with respect to virial parameters, as discussed in Sec. III A. To determine the virial spherical top-hat overdensity Δ_v, and hence the virial radius, we use a cosmology with $h = 0.7$, $\Omega_m = 0.3$, and $\Omega_\Lambda = 0.7$. We perform a set of 50 simulations, with $v_k = 10$, 50, 100, 200, and 500 km s^{-1} and $\tau = 0.1$, 1, 10, 50, and 100 Gyr, and with $c = 5$ and $c = 10$. Since the virial speed of the halo is $v_{\rm vir} \equiv \sqrt{GM_{\rm vir}/R_{\rm vir}} \approx 130$ km s^{-1} using a spherical top-hat overdensity definition of virial parameters, the kick speeds were chosen to bracket the virial value. The typical crossing time of a particle in the halo is ~ 500 Myr, and the virial time $t_{\rm vir} = R_{\rm vir}/v_{\rm vir}$ is a few Gyr, meaning that our choices for τ bracket the typical dynamical time scales of particles in the halo. We choose $c = 5$ and $c = 10$, since these are typical ΛCDM concentrations for galaxies, groups, and clusters. We use observations of such systems to set constraints on the decay parameter space in Sec. III B.

The fiducial simulations used for our analysis in Sec. III contain 1.5×10^6 particles total, or 10^6 particles within the virial radius at the start of the simulations. To test the convergence of the simulations, we run the same simulations over again but with an order of magnitude fewer particles. The convergence tests are further discussed in Sec. IV A.

We set GADGET-2 parameters, such as the softening, maximum time step, and the force accuracy criterion, according to the recommendations of Power *et al.* (2003) [36]. For the fiducial simulations, the softening length is set to 1.3 kpc, and it is set to 3.3 kpc in the low-resolution simulations. For most of the simulations, the maximum allowed time step is set to $\Delta t_{\rm max} = 10$ Myr, in accordance with Power *et al.* (2003). However, for simulations with $\tau = 100$ Myr and $\tau = 1$ Gyr, $\Delta t_{\rm max} = 1$ Myr such that $P_{\rm max} \ll 1$. We run the simulations for 10 Gyr.

We also performed simulations without decay to check that our equilibrium initial conditions were indeed in equilibrium, and to determine the extent of numerical relaxation at the halo centers. We found that the halos were stable over the 10 Gyr duration of the simulations, and that numerical relaxation ceased to be important for $r > 4$ kpc for the fiducial simulations and $r > 10$ kpc for the low-resolution simulations.

III. RESULTS

In Sec. III A, we present and summarize the results of our simulations. We show how the halo mass, NFW concentration, and NFW goodness of fit depend on the decay parameters v_k and τ, initial concentration, and time. In Sec. III B, we show how the results of the simulation can be used in combination with the observed galaxy-cluster mass

function and the halo mass-concentration relation to constrain the decay parameter space.

A. Halo profiles as a function of v_k and τ

We present the halo density profiles, multiplied by the radius to highlight differences, as a function of v_k, τ, and time in Fig. 1. We show the density profiles for halos with initial $c = 5$ since the qualitative features of the $c = 5$ and $c = 10$ halos are similar, and omit figures for $\tau = 0.1$ and 1 Gyr with $v_k = 200$ and 500 km s^{-1} since the halos are effectively destroyed within a few Gyr. The higher lines in each subplot correspond to earlier times, and the lines go (top to bottom) $t = 0$, 2.5, 5, 7.5, and 10 Gyr after the start of the simulation.

There are other interesting features of note in Fig. 1. First, we see that for small v_k relative to the virial speed, there is little change to the dark-matter profile. This is expected, as such small v_k leads to neither significant mass loss nor kinetic energy injection in the halo. However, for $v_k = 50$ km s^{-1} ($v_k/v_{\rm vir} \sim 0.4$), changes to halo structure begin to become significant for $\tau \lesssim 10$ Gyr. In general, changes to halo mass and halo structure are most extreme for large v_k and small τ. Changes are abrupt
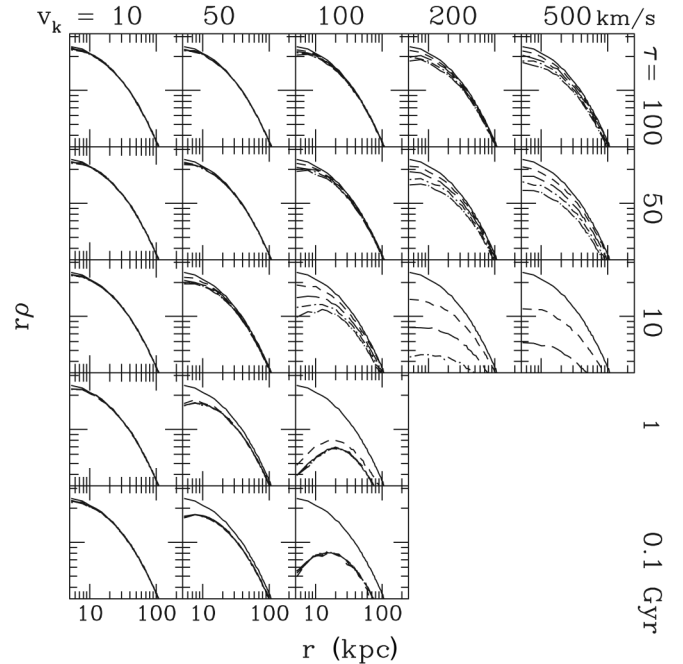

FIG. 1. The halo dark-matter density profile times the radius, as a function of radius and time. The lines correspond to different time slices in the simulation. The solid line represents the density at the beginning of the simulations; the dashed line is the density 2.5 Gyr after the simulation start; the long-dashed line is that after 5 Gyr; the dot-dashed line is the density profile after 7.5 Gyr; and the long-dash-dotted line represents the density profile after 10 Gyr. Density profiles for $v_k \gtrsim 200$ km s^{-1} and $\tau \lesssim 1$ Gyr are not shown because the halos are destroyed within a few Gyr.
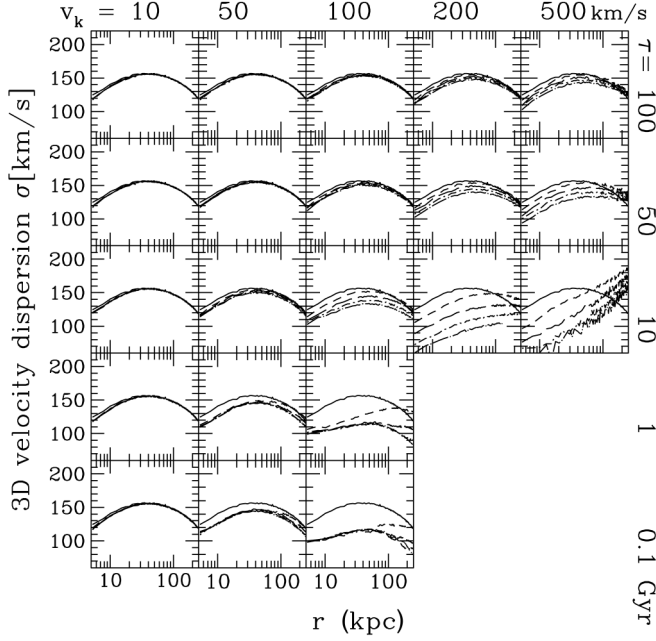
FIG. 2. The three-dimensional velocity dispersion as a function of radius and time, tiled according to v_k and τ. The lines correspond to the same time slices as in Fig. 1.
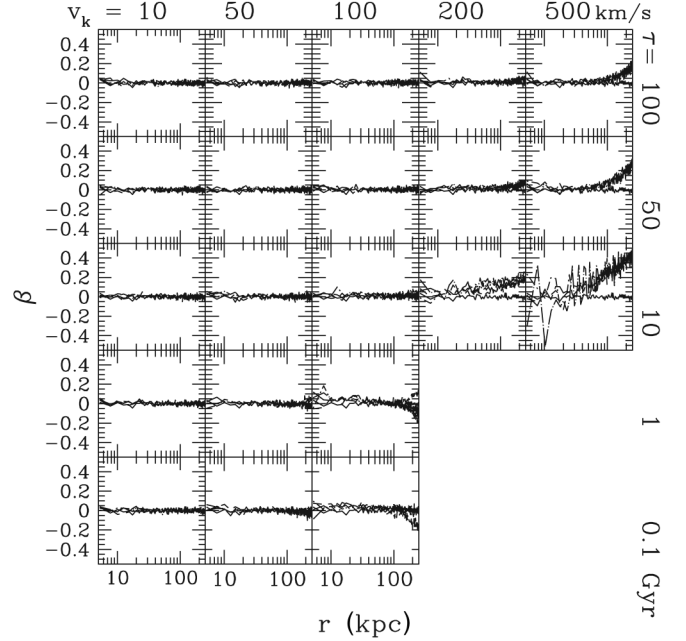

FIG. 3. The velocity anisotropy $\beta = 1 - (\sigma_\theta^2 + \sigma_\phi^2)/2\sigma_r^2$ as a function of radius and time, tiled according to v_k and τ. The lines correspond to the same time slices as in Fig. 1.

when τ is small, although it takes ~ 5 Gyr for the halos to reach equilibrium if $\tau \lesssim 1$ Gyr.

We see similar trends in the velocity data, which we present in Figs. 2 and 3. In Fig. 2, we show the velocity dispersion profiles

$$\sigma \equiv [\sigma_r^2 + \sigma_\theta^2 + \sigma_\phi^2]^{1/2} \qquad (7)$$

as a function of decay parameters and time, and in Fig. 3, we show the velocity anisotropy

$$\beta \equiv 1 - \frac{\sigma_\theta^2 + \sigma_\phi^2}{2\sigma_r^2}, \qquad (8)$$

where σ_r, σ_θ, and σ_ϕ are the velocity dispersions in spherical coordinates. We set up the initial conditions such that $\sigma_r = \sigma_\theta = \sigma_\phi$ (such that $\beta = 0$), and given the equilibrium initial conditions, the velocity dispersion is initially equivalent to the rms velocities. Even at late times in the cases of small τ or large v_k, the rms velocities are only slightly different from the velocity dispersions.

As expected, the velocity dispersion profiles $\sigma(r)$ decrease in normalization as more halo particles decay, since the negative heat capacity of a self-gravitating system ensures that an injection of kinetic energy due to decays results in an overall decrease in the equilibrium kinetic energy of the halo (cf. [25]). The most extreme drops in the velocity dispersion occur for small τ or large v_k for which the kinetic energy injected into the halos due to decays is large. The velocity dispersion profile quickly settles to a new equilibrium for $\tau \lesssim 1$ Gyr. When both v_k is large and τ is relatively small, the velocity dispersion increases as a

function of time at large r. These regions are no longer within the virial radius and contain a number of unbound particles, the latter of which, in particular, drives up the velocity dispersion.

The velocity anisotropy β hovers around zero for most times and radii of most of the decay parameters we consider. This is unsurprising, since the initial conditions and the decays have a high degree of spherical symmetry in both configuration and velocity space. The exceptions in $\beta \approx 0$ occur, unsurprisingly, for small τ and large v_k. In the case of $\tau \lesssim 1$ Gyr for $v_k = 50$ or 100 km s^{-1}, $\beta < 0$ in the outskirts of the halos at late times, indicating that orbits in the outskirts of those halos become tangentially biased. Radial orbits in the outskirts of galaxies are easiest to strip since their binding energy is lower at fixed radius than more circular orbits. For large v_k and τ, though, the orbits clearly become radially biased in the outskirts of the halo. These halos have not settled into a true dynamical equilibrium, and there is a significant net outflow of particles. This net outflow drives the radial bias in the orbits, and is more significant in the outskirts because any particle which decays onto an unbound orbit in the interior of the halo must pass through the exterior regions. Moreover, the particles originating in the outskirts are more vulnerable to ejection, so the daughter particles originating in the outskirts will also have a significant radial bias. The interior regions of the halo are less vulnerable to decay (unless $v_k \gg v_{\text{vir}}$) and the dynamical time is short relative to the decay time, both of which serve to preserve the initial orbital structure deep within the halos.

However, since the dark-matter mass profile may be inferred observationally but the dark-matter velocities are not, we focus our analysis on the mass distribution in halos as a function of decay parameters and time. Perhaps the most striking feature of Fig. 1 is that the NFW halo profile, Eq. (1), is clearly not a good fit to many of the profiles. In the way in which we have chosen to display the density profile information, $r\rho$ as a function of r, the profile should be flat for $r/r_s \ll 1$ and be monotonically decreasing for larger r. However, there is a clear turnover in $r\rho$ in some cases, most notably in the $\tau \lesssim 1$ Gyr cases, but also at late times for $\tau = 10$ or 50 Gyr and $v_k \geq 100$ km s^{-1}.

In order to find the goodness of fit of the NFW profile quantitatively, as well as the best-fit NFW parameters, we bin the particles radially with respect to the center of mass of the system, and use two different likelihood estimation routines: a simple χ^2 model, which should work in the limit of a large number of particles in each bin; and a Poisson-based likelihood. We treat the uncertainty in the number of particles in each bin as $\sqrt{N}$, where N is the observed number of particles in a bin. Instead of using ρ_s and r_s as free parameters in the NFW fit in Eq. (1), we use $M_{\rm vir}$ and c. We use 100 bins between $r_{\rm min}$ ($= 4$ kpc, the minimum radius at which numerical relaxation ceases to matter) and $r_{\rm max} = 250$ (the approximate virial radius at $t = 0$). We bin the particles either linearly or logarithmically in r, and obtain identical fits, as expected. The minimum χ^2 parameters are slightly biased relative to those obtained with the Poisson likelihood function, but not at a significant level. Thus, we can use statistics associated with χ^2 to describe the fits, and define χ^2 per degree of freedom (χ^2/d.o.f.) as our metric for the fit quality.

We summarize the best-fit NFW concentrations and the goodness of fit (parametrized by χ^2/d.o.f.) in Fig. 4. The concentrations are extrapolated to a Hubble time $t_{\rm H} = 13.7$ Gyr from our simulations, and their values correspond to the shading for each grid point representing a different

(v_k, τ) pair used for a simulation. The size of the grid points corresponds to the quality of the fit. If the χ^2/d.o.f. exceeds 1.5 at any time during the simulation, the grid point is small; if χ^2/d.o.f. < 1.5 for the whole simulation (sampled every 0.5 Gyr), then the point is large. In some cases, the fit is somewhat marginal (χ^2/d.o.f. ~ 1.5) much of the time, in the dividing regions of $v_k - \tau$ parameter space between good and really bad NFW fits. The general features between the simulations with initial $c = 5$ and $c = 10$ are similar, though; for $\tau \lesssim 10$ Gyr and $v_k/v_{\rm vir} > 0.4$ ($v_k \gtrsim 50$ km s^{-1}), the NFW profile is generally not a good fit to the halo profile at some (especially late) times. For lower v_k or high τ, the NFW density profile provides a reasonable fit throughout the lifetime of a halo, even if the halo mass and concentration change. The concentrations drop rapidly as v_k increases, and the final concentration is less sensitive, in general, to τ than to v_k. The concentration always decreases as a result of decay, which is expected if kinetic energy is injected into the halo or in the case of adiabatic expansion.

At large τ (specifically, $\tau = 50$ and 100 Gyr) and $v_k = 500$ km s^{-1}, the changes to the halo structure with time are well described by the adiabatic-expansion scheme explored in Ref. [25]. If τ is much greater than the halo dynamical time ($t_{\rm dyn} \lesssim 1$ Gyr for particles in an $M_{\rm vir} = 10^{12} M_\odot$ halo) and the kick speed is high enough that daughter particles are cleanly ejected from the halo, then changes to the gravitational potential are adiabatic and easy to model. If all particles are on circular orbits, the density profile remains constant, but with the scale radius rescaled as $r_s = r_s(t = 0)/(1 - f)$ and the NFW scale density rescaled as $\rho_s = (1 - f)^4 \rho_s(t = 0)$, where f is the fraction of the initial dark-matter particles that have decayed. We find that NFW profiles are a good fit for $v_k = 500$ km s^{-1} ($v_k/v_{\rm vir} \sim 4$) and $\tau \gtrsim 50$ Gyr with the adiabatic-expansion parameters, but this does not work so well for $\tau = 10$ Gyr or for $v_k = 200$ km s^{-1}
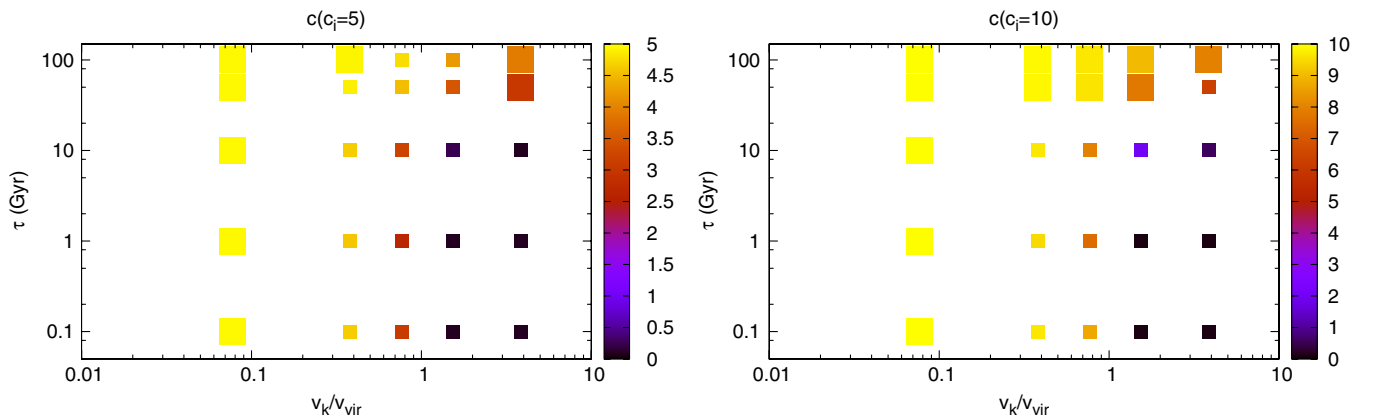

FIG. 4 (color online). Concentration at t_H for an initial $c = 5$ (left panel) and $c = 10$ (right panel). The shading indicates the NFW concentration at t_H, and the size of the points indicates the goodness of the NFW fit. Big points show that the NFW profile is a good fit to the density profile throughout the simulation, and small points indicate significant deviations from NFW fits during the simulations.

$(v_k/v_{\text{vir}} \sim 1.5)$. Thus, it appears that $\tau \gg t_{\text{dyn}}$ and $v_k/v_{\text{vir}} \gtrsim 1$ are required for the analytic adiabatic-expansion description to describe halo evolution.

We reported the goodness of fit and concentration in terms of v_k/v_{vir} instead of v_k because we would like to extrapolate the findings of our simulations to other halo masses. It is natural to parametrize the kick speeds v_k in terms of the virial speed; the virial speed is a measure of the binding energy of the halo, and v_k is a measure of the kinetic energy injected into the halo. Following Ref. [25], we link the decay time τ with the crossing time r/v_{circ} at the half-mass radius, where $v_{\text{circ}} = [GM(r)/r]^{1/2}$, such that the typical dynamical time of a particle in a halo is

$$t_{\text{dyn}} \approx (G\Delta_v\rho_m)^{-1/2}c^{-3/4}. \qquad (9)$$

Thus, we can extend our simulation results to halos of other masses.

We summarize the mass remaining after a Hubble time t_{H} in Fig. 5. In this plot, we show regions in the decay parameter space in terms of v_k/v_{vir} and τ/t_{dyn} on the left, and v_k/v_{vir} and τ on the right, in order to highlight both the absolute and relative time scales. The Hubble time is a fixed time scale, and one can consider τ in reference to that time scale, or think of t_{H} in terms of dynamical times, and then consider the relative time scale τ/t_{dyn}. The long-dashed line shows $M_{\text{vir}}(t_{\text{H}})/M_{\text{vir}}(t = 0) = 0.9$ for the $c = 5$ simulations, which has been found via interpolation of our grid of $M_{\text{vir}}(t_{\text{H}})/M_{\text{vir}}(t = 0)$ as a function of the decay parameters. This line indicates the transition from decays having little effect on the virial mass of the halo to having a nontrivial effect. The short-dashed line shows $M_{\text{vir}}(t_{\text{H}})/M_{\text{vir}}(t = 0) = 0.2$, which is around the transition between decays causing total destruction of the halo and moderate mass loss in the halo. The dotted and dot-dashed lines show $M_{\text{vir}}(t_{\text{H}})/M_{\text{vir}}(t = 0) = 0.9$ and

$M_{\text{vir}}(t_{\text{H}})/M_{\text{vir}}(t = 0) = 0.2$ for the halos which originally had $c = 10$.

When the decays are parametrized in terms of τ/t_{dyn} and v_k/v_{vir}, the $M_{\text{vir}}(t_{\text{H}})/M_{\text{vir}}(t = 0) = 0.9$ and the $M_{\text{vir}}(t_{\text{H}})/M_{\text{vir}}(t = 0) = 0.2$ lines are largely similar between the two different initial concentrations. The largest discrepancy occurs near $v_k/v_{\text{vir}} \approx 0.2$ and $\tau < 10$ Gyr. This effect is real, and is due to the fact that more concentrated halos have more particles that are more tightly bound to the halos, which makes the particles harder to eject. However, for $\tau/t_{\text{dyn}} > 10$ or for the $M_{\text{vir}}(t_{\text{H}})/M_{\text{vir}}(t = 0) = 0.2$ line, the differences in mass retention between the two sets of simulations are small. The differences are greatest at small τ/t_{dyn} and v_k/v_{vir} because the main particles affected and likely to be kicked out of the halo due to such decays are in the outer halo. If $v_k/v_{\text{vir}} \sim 1$, particles even relatively tightly bound to the halo have a high chance of being ejected, which ameliorates some differences due to differences in concentration. In general, though, even though the dynamical times of the $c = 5$ and $c = 10$ halos are different by a factor of 1.7, and even though there are different numbers of dynamical times in t_{H} for the two sets of halos, the remaining halo mass at t_{H} is not a strong function of concentration in $\tau/t_{\text{dyn}} - v_k/v_{\text{vir}}$ parameter space.

The differences are more pronounced in the right-hand side plot in Fig. 5, in which the remaining mass is plotted as a function of τ and v_k/v_{vir}. The $c = 10$ halos tend to retain more mass at fixed v_{vir} and τ because the typical particle has a higher binding energy than in the $c = 5$ case. Since the dynamical time depends on c, which is related to the distribution of particle energies within the halo, some of the dependence of halo mass loss on concentration is divided out by parametrizing mass loss in terms of τ/t_{dyn} instead of τ.
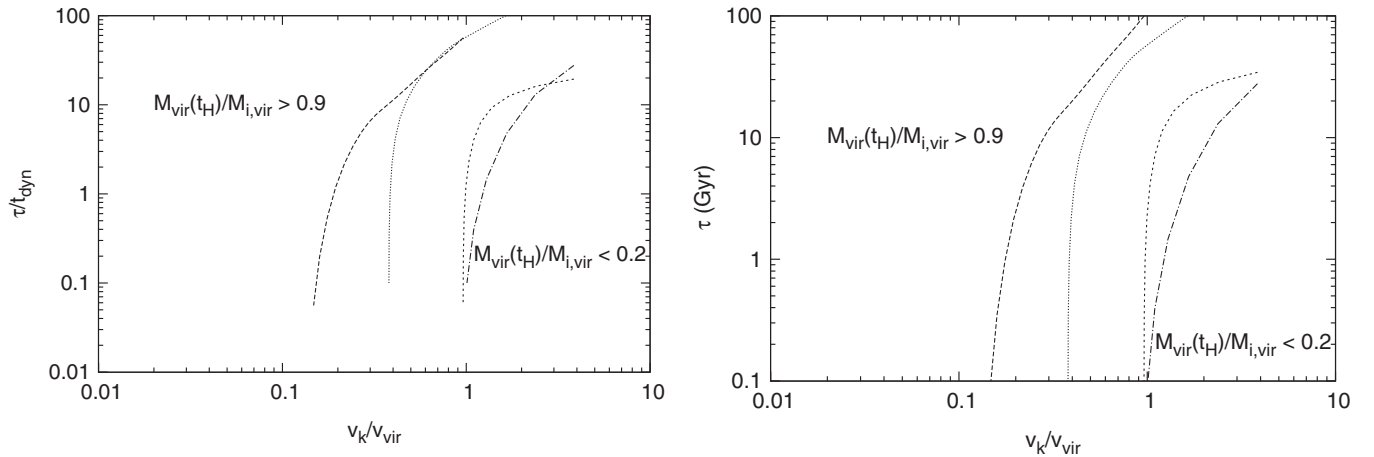

FIG. 5. Virial mass remaining at $z = 0$ as a function of the initial concentration, τ, and v_k. The long- and short-dashed lines show where the virial mass after a Hubble time is 0.9 and 0.2, respectively, times the initial virial mass if the initial concentration is $c = 5$. The dotted and dot-dashed lines show the equivalent 0.9 and 0.2 remaining mass fractions for an initial $c = 10$. Left panel: Remaining mass as a function of τ/t_{dyn} and v_k/v_{vir}. Right panel: Remaining mass as a function of τ in Gyr and v_k/v_{vir}.

A more direct comparison would be to examine mass loss and concentration changes as a function of v_k/v_{vir} and τ/t_{dyn} for a fixed number of dynamical times. When we do this, we find that the $M_{vir}(t_H)/M_{vir}(t=0) = 0.2$ lines lie practically on top of each other for $c = 5$ and $c = 10$, but the $M_{vir}(t_H)/M_{vir}(t=0) = 0.9$ line is offset by approximately a factor of 2 in τ/t_{dyn} between $c = 5$ and $c = 10$. However, what matters in comparisons to observations is the effect of decay at a fixed time. Instead of mapping results in terms of v_k/v_{vir} and τ/t_{dyn}, we interpolate in terms of v_k/v_{vir}, τ, and c. Our simulations span the typical ΛCDM concentrations expected for the sizes of halos relevant to the observations, and the virial speeds span a factor of ≈ 10, a relatively small range.

In summary, we find that for halos that initially have $c = 5$ or 10 and have the equilibrium NFW halo profiles expected in ΛCDM simulations, the effects of decay in the regime $\tau/t_{dyn} \lesssim 10$ and $v_{vir}/v_k \gtrsim 1$ are to drastically lower the halo concentration in a Hubble time, drive substantial mass loss, and drive changes to the halo profile such that the NFW profile is not a good fit. For $\tau/t_{dyn} \gtrsim 50$ Gyr or $v_k/v_{vir} \lesssim 0.2$, the NFW profile remains a good fit to the density profile, mass loss is not too significant, and the concentration does not drop too much. Mass loss and concentration reduction are more severe for fixed τ/t_{dyn} for large v_k until $v_k/v_{vir} \sim 4$, at which point the decay can be described analytically in the adiabatic-expansion approximation, and the effects of decay no longer depend on v_k as long as $v_k/v_{vir} \gtrsim 4$. At such high v_k, any daughter particle in a decay is ejected from the halo, so there is no kinetic energy injection into the halo as a result of decays. In the intermediate regime [roughly corresponding to the space between the $M_{vir}(t_H)/M_{vir}(t=0) = 0.2$ and $M_{vir}(t_H)/M_{vir}(t=0) = 0.9$ lines], mass loss is moderate although the concentration may drop quite a lot, and the inner part of the density profile is shallower than for NFW.

There are some differences between the $c = 5$ and $c = 10$ simulations beyond that which can be factored out by parametrizing decay in terms of the virial time scales v_k/v_{vir} and τ/t_{dyn}. This is due to the fact that the gravitational potential, and hence binding energy, does depend on the concentration in a way that is not completely factored out by the virial scaling. Even though we parametrize halos in terms of "typical" dynamical times and typical speeds, there is a diversity of particle speeds and time scales within a halo. Nonetheless, since our simulations span the range of t_{dyn} and c of the halo observations below, we are able to interpolate our simulations and map ΛCDM dark-matter halos to halos in a decaying-dark-matter cosmology.

B. Relation to observational constraints

1. The mass-concentration relation

Under the hierarchical picture of structure formation in the Universe, it is expected that low-mass dark-matter halos form earlier than high-mass halos. As a consequence of this early formation time, the inner parts of low-mass halos are far more dense relative to the outskirts of the halo relative to high-mass halos [37]. In other words, low-mass halos are more concentrated than high-mass halos. This trend has been observed and quantified in simulations of ΛCDM cosmologies [38–43]. It is found that cosmologies with higher matter fractions, Ω_m, and a higher amplitude of matter fluctuations averaged in $8h^{-1}$ Mpc spheres, σ_8, produce higher concentrations for fixed halo mass than cosmologies in which Ω_m and σ_8 are low. This is due to the fact that structures collapse earlier when the Universe is more dense if Ω_m and σ_8 are higher.

Decays will make halos appear less concentrated; hence, Ω_m and σ_8 inferred from halos that have experienced decay *if* one begins with a WIMP dark-matter ansatz would be lower than that inferred from observations of earlier epochs. We can set conservative constraints on the decay parameter space by comparing observationally inferred mass-concentration relations with the mass-concentration relation derived from decays in a high-Ω_m, high-σ_8 cosmology. The CMB last-scattering surface is the earliest window into cosmological parameters. The six-parameter cosmological fit to the *Wilkinson Microwave Anisotropy Probe* (WMAP) seven-year data set suggests $\Omega_m = 0.267 \pm 0.026$ (1-σ) and $\sigma_8 = 0.801 \pm 0.030$ (1-σ) [44]. The 2-σ upper limits of Ω_m and σ_8 correspond approximately to the mean WMAP first-year mean parameters [45]. The mean mass-concentration relation found in simulations of a ΛCDM cosmology using the WMAP-1 parameters is illustrated in Fig. 6, and is denoted by the upper solid line [42].

We use our grid of mass loss and concentration as a function of τ and v_k/v_{vir}, found using the simulations and described in Sec. III A, to map ΛCDM halo masses and concentrations in a WMAP-1 cosmology to those of halos at $t = t_H$. We show the mass-concentration relation as a function of decay parameters in Fig. 6, along with the mean theoretical and observed relations. It should be noted that we use the best-fit NFW concentrations [Eq. (2)] in Fig. 6, even if the NFW profile is not a good fit to the density profile. Nonetheless, the NFW concentration provides a reasonable measure of the density contrast within the halo.

In Fig. 6, the solid lines represent the mean mass-concentration relations found in dissipationless, baryon-free cosmological simulations using WMAP one-year (upper line) [45] and WMAP three-year (bottom line) [46] cosmologies [42]. The long-dashed lines represent decaying-dark-matter models with (top to bottom) $\tau = 100$, 40, 20, and 5 Gyr under the assumption that the WMAP one-year cosmology is the underlying cosmology. The short-dashed and dotted lines are observationally inferred mean mass-concentration relations using a sample of clusters observed in a variety of ways [47] and x-ray observations [48], respectively. The error bar in the upper
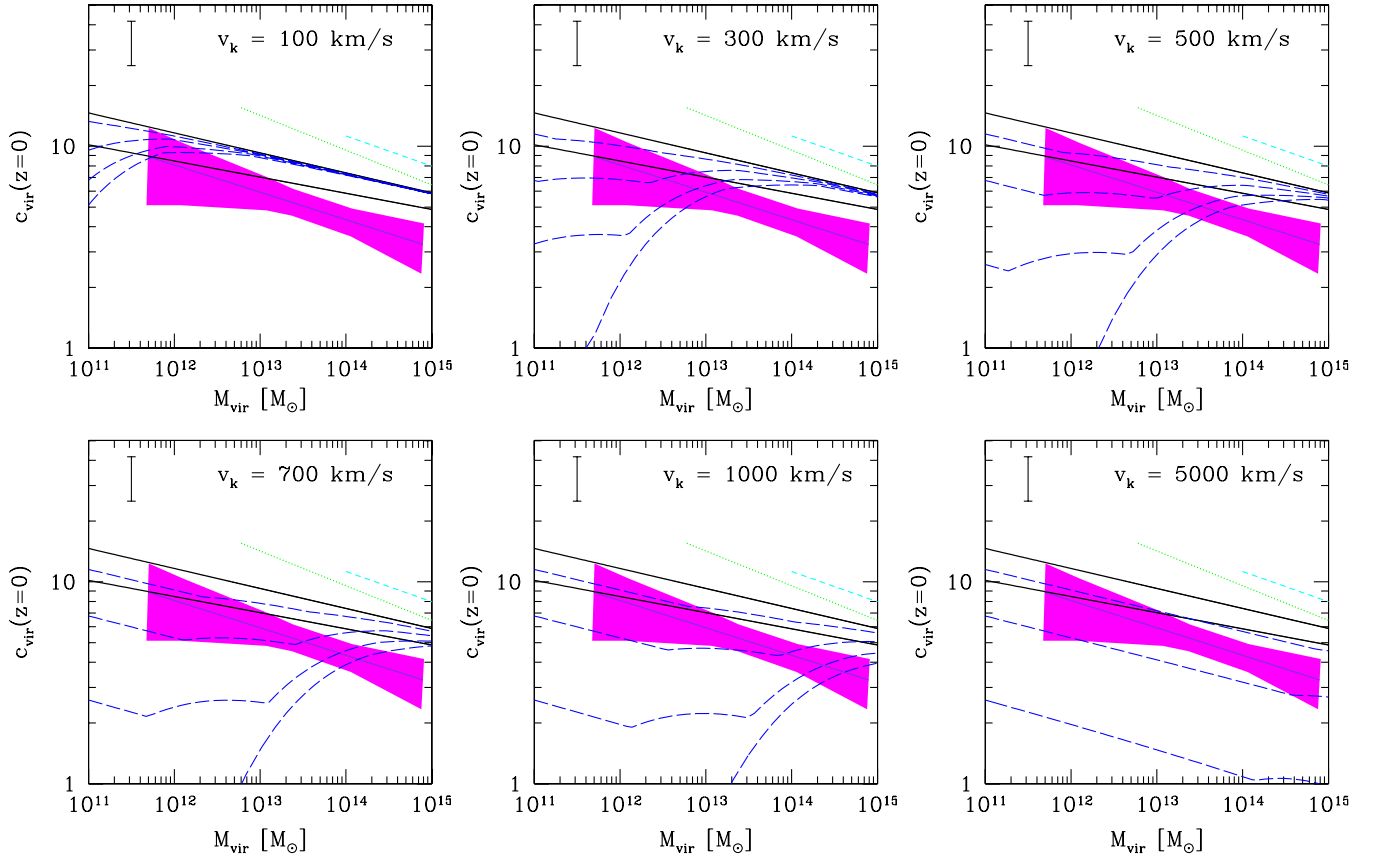
FIG. 6 (color online). The mass-concentration relations predicted for ΛCDM and decaying-dark-matter cosmologies and inferred from observations of galaxies, galaxy groups, and clusters. The short-dashed line shows the mean mass-concentration relation found in Ref. [104] using cluster observations, and the dotted line shows that from x-ray observations in Ref. [48]. The shaded region shows the 1-σ fits to the mean mass-concentration relation inferred from weak lensing [49]. The upper and lower solid lines show the mean mass-concentration relation found in dissipationless simulations using WMAP-1 and WMAP-3 cosmological parameters, which bracket the WMAP-7 mass-concentration relation [42]. The long-dashed lines show the mass-concentration relation for decaying dark matter, with the lines corresponding to (from thickest to thinnest) $\tau = 5, 20, 40,$ and 100 Gyr. The error bar shows the intrinsic scatter in the theoretical relations, and is also approximately the 1-σ error in the mean observationally inferred relations.

left corner of the plots shows the scatter in the mass-concentration relation for simulations, and the typical uncertainty in the mean mass-concentration relation from the observations. The shaded region corresponds to the 1-σ region of the mean mass-concentration relation inferred from weak-lensing observations of Sloan Digital Sky Survey (SDSS) galaxies [49].

We use only the weak-lensing mass-concentration relation to constrain the decay parameters. This is because the cluster and x-ray samples have serious selection effects which have not been fully quantified. Reference [47] finds that the concentration of strong-lens clusters is even higher than that predicted by Ref. [50], who identified strong-lens systems in N-body simulations. Dark-matter profiles can only be inferred from x-ray observations if the halos are relaxed; relaxed halos have, on average, higher concentration than the population of halos as a whole [39]. Thus, until the selection effects are better quantified for the x-ray

and strong-lens systems, one should not use the mass concentration inferred from observations of those systems to constrain dark-matter models.

Even though there are also systematics that have not been fully quantified in the weak-lensing measurement (see Sec. IIID of Ref. [49] for a sampling of possible effects), the measurement provides conservative constraints because it lies slightly below simulation values, on which we base our decay predictions. We consider a (v_k, τ) pair of parameters to be excluded if its mass-concentration relation lies below the 1-σ lower limit of the mean weak-lensing mass-concentration relation.

Using this criterion, we see from Fig. 6 that current weak-lensing measurements are unable to constrain τ for $v_k \lesssim 100$ km s^{-1}. However, $\tau \lesssim 30$ Gyr is ruled out for 300 km s$^{-1} \lesssim v_k \lesssim 700$ km s^{-1}, and $\tau \lesssim 35$–40 km s^{-1} for larger values of v_k. Interestingly, the constraints from the simulations for large v_k are nearly identical to those

found analytically using a simple model of adiabatic expansion (valid only if $\tau/t_{\text{dyn}} \gg 1$ and $v_k/v_{\text{vir}} \gg 1$) in Ref. [25].

We have neglected the effects of baryons on the halo concentration. This is largely because it is not clear how baryons affect the dark-matter halo. In cosmological simulations with two different prescriptions for baryon physics, Rudd *et al.* (2008) [51] found either little difference relative to dark-matter-only simulations, or an increase in concentration of $\sim$50% above the dark-matter-only values. However, even in the latter case, the minimum allowed τ for fixed v_k would only decrease $\sim$15%–30%.

Better constraints may be obtained in the future. Upcoming deep wide-field surveys will increase the statistics of weak and strong lensing and x-ray cluster profiles, and probe down to smaller halo masses [52–55]. However, improvements in using the (redshift-dependent) mass-concentration relation to constrain dark-matter decays (or cosmological parameters) will require a better understanding of the systematics and selection effects for the various methods of measuring the dark-matter halo masses of galaxies and clusters. This is likely to be a subject of significant future work, since the selection effects are relevant to determining halo mass functions. The evolution of halo mass functions depends on the growth function. Since the growth function is sensitive to the equation of state of dark energy, there will be significant efforts to understand any systematic errors that may obscure inferences about dark energy from observations [56]. In addition, there needs to be a better theoretical understanding of which processes of galaxy evolution drive changes to dark-matter halo profiles. This subject has generated recent interest [57–61], and with continuing improvements in the spatial resolution and star-formation and feedback recipes in simulations, it should be possible to determine which physical processes influence the distribution of dark matter within galaxies.

2. Galaxy-cluster mass functions

The mass function of galaxy clusters $n(>M_{\text{vir}})$ is sensitive to Ω_m and σ_8 for similar reasons as for the mass-concentration relation; if the amplitude of matter fluctuations is higher, structure forms earlier and is more abundant in the local Universe [62–66]. Since galaxy clusters are the largest and rarest of virialized structures, corresponding to small fluctuations in the linear matter density field smoothed on $\sim$10 Mpc scales, small changes in σ_8 and Ω_m will result in large changes to the cluster mass function.

If dark matter were to decay into relativistic particles, the cluster mass function would look different than the ΛCDM mass function because the continuous pumping of relativistic particles into the Universe would alter the background evolution of the Universe and, hence, the density threshold for halo collapse. This effect was inves-

tigated by Oguri *et al.* (2003) [67]. However, the main effect of decays in which the mass splitting between dark-matter species is small is to reduce the mass of halos due to ejection resulting from decays. Since σ_8 and Ω_m should be the same regardless of the redshift of the matter tracer in a ΛCDM universe, the smoking gun for decays would be if Ω_m and σ_8 inferred from an early epoch (the cosmic microwave background or Lyman-α forest) were systematically higher than that inferred from the $z = 0$ cluster mass function.

We use parameter estimates from the WMAP seven-year data set and low-redshift observations of clusters to constrain decay parameter space. As with the analysis using the mass-concentration relation, we find conservative bounds on the decay parameter space by considering the parameters for which the cluster mass function with Ω_m and σ_8 set to 2-σ above the WMAP-7 parameters maps to a cluster mass function that is 1-σ below Ω_m and σ_8 inferred from observations of low-redshift clusters. Both optical and x-ray observations of clusters indicate that the 1-σ lower limits on Ω_m and σ_8 are approximately the same as the 2-σ lower limits on those parameters from WMAP-7, $\Omega_m \approx 0.2$ and $\sigma_8 \approx 0.7$ [3,5,68–71].

We use the relation between the ΛCDM halo masses and the halo masses after $t = t_{\text{H}}$ with decay to find the cluster mass function,

$$n_f(>M_f) = \int_{M_f}^{\infty} dM_f' \frac{dn_i(M_i(M_f'))}{dM_i} \frac{dM_i}{dM_f'}. \qquad (10)$$

Here, $n_f(>M_f)$ is the comoving number density of halos with masses larger than M_f after a Hubble time of decay, dn_i/dM_i is the Tinker *et al.* (2008) [72] ΛCDM differential mass function, M_i is the initial ΛCDM mass of the halos, and M_f is the final halo mass after a Hubble time of decay. Since the relation between M_i and M_f masses depends on concentration (Sec. III A), we use the WMAP-1 mass-concentration relation from Ref. [42] to set the initial concentrations of the initial ΛCDM halos and interpolate among our simulations to find M_f from M_i.

We show the galaxy-cluster mass function as a function of decay parameters in Fig. 7. The dotted line is the mass function for the high-Ω_m, high-σ_8 cosmology, the solid line is for the mean WMAP-7 cosmology, and the long-dashed line represents the mass function for a cosmology set to the 2-σ lower limits of Ω_m and σ_8 parameters from WMAP-7 from the six-parameter cosmological fit [44]. All other cosmological parameters have been set to the WMAP-7 mean values, as those parameters do not affect the normalization or shape of the mass function nearly as much as Ω_m and σ_8. The short-dashed lines show the mass functions assuming (top to bottom) $\tau = 100, 40, 20,$ and 5 Gyr. Each panel shows a different v_k.

It is clear that the cluster mass function (for which we consider $M_{\text{vir}} \gtrsim 10^{14} M_\odot$ to be classified as a cluster) is
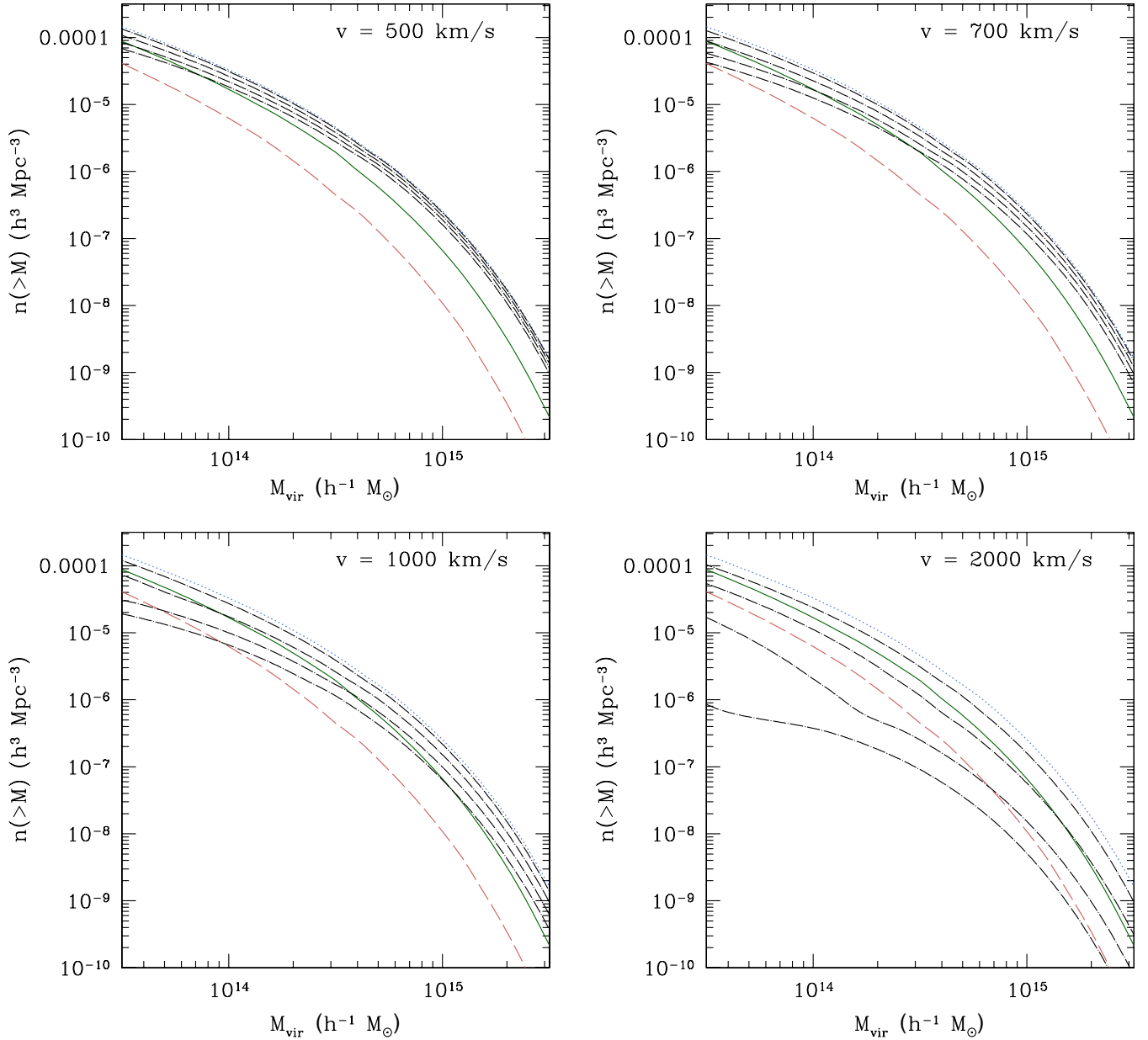
FIG. 7 (color online). $z = 0$ cluster mass functions. In each panel, the dotted (blue) line represents the Tinker *et al.* (2008) [72] mass function for a cosmology with $\Omega_m = 0.318$ and $\sigma_8 = 0.868$, but with all other parameters set to the mean values found in the six-parameter fit of the WMAP-7 data [44]. The solid (green) line represents the WMAP-7 six-parameter mean cosmology, and the long-dashed (red) line represents a cosmology with $\Omega_m = 0.198$ and $\sigma_8 = 0.724$. The short-dashed (black) lines show cluster mass functions for a cosmology with $\Omega_m = 0.318$ and $\sigma_8 = 0.868$, but with decaying dark matter with (bottom to top) $\tau = 5, 20, 40,$ and 100 Gyr. For clarity, each panel shows a different v_k.

relatively insensitive to small kick speeds, $v_k \lesssim 500$ km s^{-1}. This is because the typical virial speed of a cluster is $v_{\rm vir} \gtrsim 600$ km s^{-1}. From Fig. 5, it is apparent that severe mass loss in dark-matter halos requires $v_k/v_{\rm vir} \gtrsim 1$ and $\tau \lesssim 10$ Gyr. However, the shape of the mass function is somewhat different than those predicted in ΛCDM cosmologies, since higher mass halos are less affected by lower v_k than low-mass halos. For $v_k = 1000$ km s^{-1}, the number density of $M_{\rm vir} > 10^{14} M_\odot$ is

approximately the same for τ as the lowest number density allowed by low-redshift observations of clusters. However, even for higher τ, the cluster mass function is far less steep than predicted by ΛCDM. At $v_k = 2000$ km s^{-1}, the cluster number density is too low for $\tau \lesssim 30$ Gyr. At even higher v_k, the cluster mass functions converge to the analytic estimates of Ref. [25] in the case of $v_k/v_{\rm vir} \gg 1$, and constrain $\tau \gtrsim 35$–40 Gyr. The shape of the cluster mass function as well as the number density $n(>10^{14} M_\odot)$

can be used to constrain decays, but the statistics are generally lower for higher cluster masses.

Constraints on dark-matter decays from the cluster mass function are more robust to baryon physics than the mass-concentration relation. Using N-body hydrodynamic simulations with two different models for baryon physics, Rudd *et al.* (2008) [51] found that the normalization of the halo mass function deviates by $\lesssim 10\%$ with the inclusion of baryons relative to the halo mass function found in N-body cold-dark-matter-only simulations.

The redshift evolution of the cluster mass function is also a useful probe of decays [25]. The signature of decays will be that, for a fixed $z = 0$ mass function, the high-redshift mass functions will have higher normalization and a different shape than in a ΛCDM universe. If one were to estimate Ω_m and σ_8 for different redshift slices with the ansatz of a ΛCDM universe, one would estimate systematically higher σ_8 and Ω_m at higher redshifts. Currently, σ_8 and Ω_m inferred from small samples of x-ray clusters up to $z = 0.7$ are consistent at different redshift slices, although the error bars are still fairly large [3,68,70,71]. Upcoming deep optical, x-ray, and Sunyaev-Zel'dovich surveys [52–55,73–75] should allow for better constraints on decays, since they will find large samples of clusters at a variety of redshifts.

C. Summary

We summarize the constraints on the decaying-dark-matter parameter space in Fig. 8. The exclusion region, marked "ruled out" on the plot, comes from three types of observations. For relativistic v_k, the WMAP-1 data set the strongest constraint on τ, with $\tau \gtrsim 123$ Gyr at 68% C.L. [76]. This restriction is essentially a restriction on $\rho_r(z)$, the radiation density of the Universe as a function of time.
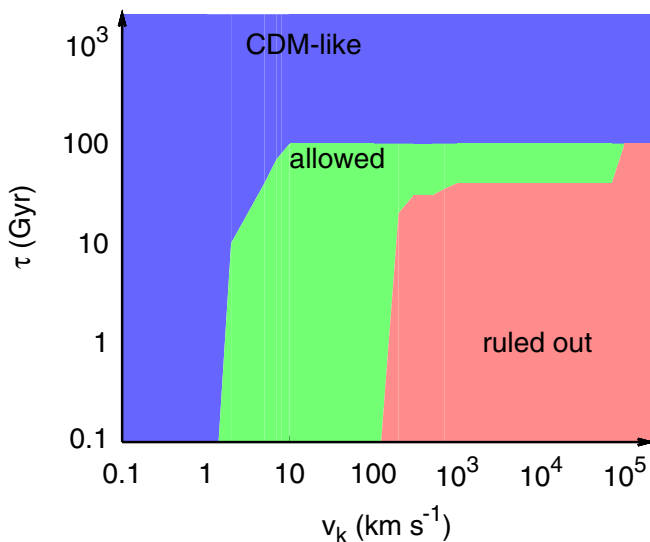

FIG. 8 (color online).   Summary of the mass-concentration and $z = 0$ cluster mass function limits on the decay parameter space.

For $v_k \gtrsim 2000$ km s^{-1}, both the galaxy-cluster mass function and the mass-concentration relation require $\tau \gtrsim 40$ Gyr. At lower v_k, the mass-concentration relation sets best constraints on τ, at approximately the level $\tau \gtrsim 30$ Gyr for 300 km s$^{-1} \lesssim v_k \lesssim 700$ km s^{-1} and $\tau \gtrsim 20$ Gyr for 100 km s$^{-1} \lesssim v_k \lesssim 300$ km s^{-1}.

We note that this exclusion region looks similar to that of Ref. [25]. However, the exclusion region in this paper is more robust; the exclusion region for $v_k \lesssim 5000$ km s^{-1} in Ref. [25] was based on noting that the clustering of galaxies in the SDSS appeared to be consistent with the clustering of ΛCDM halos with $M_{\rm vir} \gtrsim 10^{12} M_\odot$ [77]. The constraint was set based on not letting ΛCDM halos with $M_{\rm vir} \sim 10^{12} M_\odot$ lose more than half their mass due to decays. This is a fairly hand-waving constraint. It will likely take cosmological simulations of decaying dark matter in order to map galaxy clustering to constraints on dark-matter decays.

The regions labeled "CDM-like" ("cold-dark-matter-like," such as WIMPs) and "allowed" are still plausible regions of parameter space. However, it will be challenging to probe the region marked "CDM-like." For $\tau \gtrsim 100$ Gyr, there is hardly any change to halo properties; mass loss relative to ΛCDM halos is on the $\sim 10\%$ level, and concentrations go down by at most $\sim 20\%$. The NFW profile is still a reasonable fit to the halo density profiles. It is not clear if the systematics in even the largest and deepest all-sky surveys will be small enough to probe such subtle deviations from ΛCDM halo properties. Decay models with $v_k \lesssim 1$ km s^{-1} will also be challenging to probe, as such speeds are far less than the typical virial speeds of galaxies or larger systems. The smallest halos that have been found observationally have $M_{\rm vir} \sim 10^9 M_\odot$, and are subhalos at that [78,79]. Such halos have $v_{\rm vir} \approx 13$ km s^{-1}. As we saw in Sec. III A, the structural properties of dark-matter halos hardly change if $v_k/v_{\rm vir} \ll 1$. Moreover, there are poor statistics of such small halos, and it is not clear how many halos of that size will host a luminous component. The statistics of such small objects may be probed using gravitational milli-lensing, but we are years away from building any sort of statistical sample of such halos [80–82].

There is some hope of further constraining the region marked allowed in the near future. Sunyaev-Zel'dovich, x-ray, and deep optical surveys should uncover $\sim 10^5$ galaxy clusters up to quite high redshift [52–55,74,75]; then, both the $z = 0$ cluster mass function and the evolution of the cluster mass function could be used to more accurately constrain the decay parameter space. The deep optical surveys should also allow for a more precise measurement of the mean mass-concentration relation, and down to lower halo masses. On the theoretical side, a better understanding of selection effects will allow for a better comparison of the decaying-dark-matter predictions with observations. In addition, if cosmological simulations of

decaying dark matter are performed, one can hope to characterize the halo occupation distribution (HOD) [77,83–87], which will open up galaxy clustering as an avenue to better explore the decay parameter space.

So far, we have not explored using dwarf galaxies to constrain the allowed region of parameter space, as suggested by Ref. [24]. This is because there are no robust measurements of the abundance of $M_{\rm vir} \lesssim 10^{11} M_\odot$ halos, nor are there strong constraints on the inner profiles of dwarf galaxies [88–91].[1] One could imagine that the $M_{\rm vir} \sim 10^9 M_\odot$ dwarf galaxies could be the result of decays of halos born with much higher virial masses, although the density profile would be significantly different than expected in ΛCDM. In the future, large optical surveys such as the Large Synoptic Survey Telescope will look farther down the luminosity function, both in the Local Group and in the local universe [54,92], which will allow for better constraints using the abundance of low-mass halos. Astrometric observations of stars in Local Group dwarf galaxies will be critical getting the three-dimensional stellar kinematic velocity data for better constraints on the dark-matter density profiles in those galaxies [89]. This will be possible with next-generation astrometric satellites, such as *Gaia* and SIM [89,93].

IV. DISCUSSION

In the previous section, we presented the results of our simulations and showed how those results, along with the mass-concentration relation and cluster mass functions inferred from existing observations, could be used to constrain the decaying-dark-matter parameter space. In this section, we address two issues that will affect future attempts to further constrain the decay parameter space: numerical convergence in simulations, and more accurate mapping of simulations to observations.

A. Resolution effects

We based all our analysis in Sec. III on simulations that initially had $\sim 10^6$ particles within the virial radius. We would like to know which of the results we described above are fully converged, and which results may be spurious due to resolution effects. Moreover, we would like to understand resolution effects before embarking on cosmological simulations, which are far more costly than the simulations described in Sec. II. If $\gtrsim 10^6$ particles are required within a virial radius in order to determine halo properties, it becomes prohibitive to get good statistics on

---

[1]We also disagree with several of the technical aspects of Ref. [24]: (1) The mechanical kinetic energy injected by the kick velocity is far more important than the change in the rest-mass energy they consider. (2) Our analysis shows that the preservation of a NFW profile, assumed therein, is not valid. (3) We find that halos may undergo disruption even for $v_k \lesssim v_{\rm vir}$.
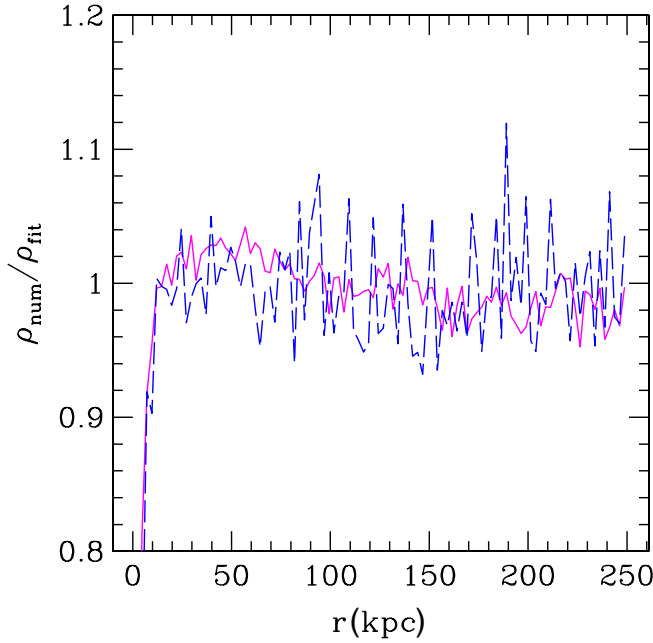
dark-matter halos (and subhalos) on a variety of mass scales in cosmological simulations.

In order to understand the robustness of our results, and to determine if one can get away with fewer particles in the virial radius for cosmological simulations, we perform simulations with the same c, v_k, and τ values as those used in Sec. III, but with 10^5 particles within the virial radius. The low-resolution simulations are briefly described in Sec. II. Our goal is to determine how the virial mass, concentration, and goodness of fit to the NFW density profile compare between the two sets of simulations.

We find that the virial mass derived from fits to the NFW profile are consistent between the two sets of simulations, and are consistent with the virial mass as determined by finding the average density of dark-matter particles within a sphere centered on the halo center of mass. Similarly, the NFW concentration parameter from the fits is also consistent between the two sets of simulations. Therefore, if one is concerned with accurately determining halo masses or NFW concentration parameters in a simulation with a decaying-dark-matter cosmology, one requires no more than 10^5 particles within the virial radius.

By contrast, the quality of the NFW fit can be sensitive to the number of particles within the virial radius. For example, $\chi^2/{\rm d.o.f.} < 1.4$ for fits to all particles within the virial radius for $v_k = 100\ {\rm km\,s^{-1}}$ and $\tau = 10\ {\rm Gyr}$ for 10^5 particles within the virial radius, regardless of the initial concentration. However, the χ^2 is bad for $t > 0.5\ {\rm Gyr}$ for both $c = 5$ and $c = 10$ if there are initially 10^6 particles in the virial radius, even though the NFW fit parameters of the two different-resolution simulations are identical (see Fig. 10 for χ^2 in the $c = 10$ case). This is illustrated in Fig. 9, in which we show the density profile from the simulation ($\rho_{\rm num}$) divided by the best-fit NFW profile for the two simulations at $t = 9\ {\rm Gyr}$ with $c = 10$, $v_k = 100\ {\rm km\,s^{-1}}$, and $\tau = 10\ {\rm Gyr}$ ($\rho_{\rm fit}$). The innermost points ($r \lesssim 10\ {\rm kpc}$) show evidence of numerical relaxation. For the rest of the halo, one can tell that there is significant curvature in $\rho_{\rm num}/\rho_{\rm fit}$ for the 10^6-particle simulation, but not for the 10^5-particle simulations. This difference is likely in large part due to the increased Poisson noise in the 10^5-particle simulation. In general, the discrepancy in the quality of the fit appears to be exacerbated in cases in which $\tau \lesssim 10\ {\rm Gyr}$ and $v_k/v_{\rm vir} \lesssim 1$.

The consequences for our results are as follows. Our constraints on the decay parameter space from cluster mass functions depended on the mapping between the ΛCDM halo mass and the halo mass after a time $t_{\rm H}$. The mass estimated in the high-resolution simulations used in Sec. III is virtually identical to that found in the lower-resolution simulations, so we believe the halo mass (as a function of decay parameters and time) to be converged and reliable. Similarly, the use of the mass-concentration relation depends on the mapping of ΛCDM halo masses

FIG. 9 (color online). Density profile for the $c = 10$, $v_k = 100$ km s^{-1}, $\tau = 10$ Gyr simulations at 9 Gyr divided by the best-fit NFW density profile. Solid line: 10^6 particles in the virial radius. Dashed line: 10^5 particles within the virial radius.

FIG. 10 (color online). NFW fits to a simulation of a $10^{12}M_\odot$, $c = 10$ halo with $v_k = 100$ km s^{-1} and $\tau = 10$ Gyr. The solid line represents a fit using all data down to the inner cutoff (4 kpc), the short-dashed line represents fits using particles within half of the initial virial radius, the long-dashed line shows fits within the inner tenth of the initial virial radius, and the dot-dashed line shows fits to the outer half of the halo. The error bars are the 90% limits from bootstrap resampling particles at each time step, although the error bars lose meaning as the χ^2 becomes large. Top panel: NFW fits to the virial mass. The true virial mass follows the solid line. Middle panel: The NFW concentration. Bottom panel: χ^2/d.o.f. for the NFW fit.

and NFW concentrations to those of halos that have experienced decays. Again, we believe the virial masses and NFW concentrations to be converged in our simulations. The shape of the dark-matter density profile is not used for mapping either of the observations to constraints on decay parameter space. Thus, we believe the mapping of our simulations to observational constraints to be robust.

The implications for future cosmological N-body simulations are as follows. We believe it is possible to get accurate estimates of halo masses and NFW concentrations using no more than $\sim 10^5$ particles in the virial radius. It may be possible to get good statistics using fewer particles, but it will likely take convergence tests in fully cosmological N-body simulations to determine the minimum particle number required for convergence, especially for subhalos. This means that it may be possible to explore decaying-dark-matter cosmologies with reasonable statistics using modest computational resources. The only situation in which higher particle numbers may be required is a detailed comparison of the shape of decaying-dark-matter halo profiles with respect to ΛCDM halos. In this case, we showed that $\sim 10^6$ particles are required within the virial radius to determine the goodness of the NFW fit, at least down to $\sim 0.02R_{\rm vir}$ for $v_k/v_{\rm vir}$ and $\tau \lesssim 10$ Gyr. In other regions of the decay parameter space, the 10^5- and 10^6-particle simulations converge on the goodness of the NFW fit. If one is mainly concerned with radical differences between ΛCDM and decaying-dark-matter halo density profiles, then $\sim 10^5$ particles within the virial (or tidal
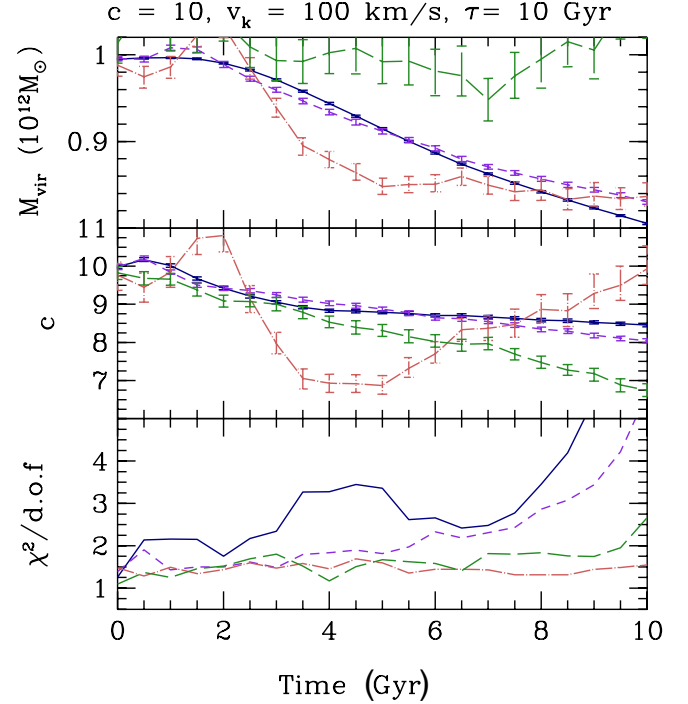
truncation) radius is likely sufficient; more subtle differences require higher particle numbers.

B. Mapping simulations to observations

In Sec. III, we used NFW fits to the entire halos to relate halo properties to observables. However, astronomical probes of the gravitational potential of galaxies and their halos are rarely sensitive to the entire halo. Rotation curves rarely extend beyond the inner 10%–20% of the virial radius of the halo [94–96], strong lensing is generally also most sensitive to the mass within $\sim 10\%$–20% of the virial radius [97–99], and weak lensing is generally most sensitive to the outer parts of halos (excluding the inner $\sim 20\%$ of the virial radius) [98,100]. X-ray gas profiles in galaxies, groups, and clusters can extend up to several tens of percents from the halo centers [101,102]. If dark-matter halos were well described by the NFW profile and there were no systematics in the observations that would bias the determination of the dark-matter profile, then all probes should yield the same profile fits.

Different probes sometimes yield different profile fits, though. For example, it has been claimed that NFW fits to dwarf-galaxy rotation curves trend lower in concentrations than predicted in dissipationless cold-dark-matter simulations, and that NFW profiles are not always good fits to the data [42,96]. Strong-lens systems and X-ray clusters appear to have higher concentrations than the average concentrations predicted by simulations, although a large part of that may be due to selection effects [50,103]. In some cases, multiple probes are used on the same system and show different fits. For example, Ref. [98] found moderate tension between the weak-lensing and strong-lensing NFW fits to Abell 611 (although the mass contained within 100 kpc, which is approximately the transition point between the domains of the probes, is consistent), and strong tension with NFW fits derived from stellar kinematic data, so much so that density profiles significantly shallower than NFW are preferred if the three data sets are combined [98].

We would like to explore the possibility that these discrepancies could be explained in the context of decaying dark matter. In Sec. III B, we showed that the NFW profile is not always a good fit to dark-matter halos after some of the X particles have decayed, especially if $v_k/v_{\rm vir} \sim 1$. Thus, profile fits to subsections of the halo may deviate from fits to the whole halo.

To demonstrate trends in the fit parameters as a function of where in the halo one performs the fit, we show in Fig. 10 NFW fit parameters and the goodness of fit (χ^2/d.o.f.) as a function of time for a halo initially in equilibrium with $M_{\rm vir} = 10^{12} M_\odot$ and $c = 10$, with $v_k = 100$ km s^{-1} and $\tau = 10$ Gyr. The solid (blue) line shows the NFW fit parameters $M_{\rm vir}$ and c using all particles within the virial radius. The error bars indicate the 90% range of parameter fits based on bootstrap resampling particles at each time slice. The short-dashed line shows the best-fit parameters using only those particles in the inner half of the virial radius, and the long-dashed line shows the fits to particles within the inner 10% of the virial radius. In these three cases, the inner cutoff to the fits is 4 kpc, corresponding to the minimum radius at which numerical effects on the density profile can be ignored. The dot-dashed line shows the fit resulting from considering only those particles with radii $>0.5R_{\rm vir}$. In many cases, the NFW profile does not provide a good fit to the density profiles, but it is also not always a good fit to observational data. The trends we discuss below are there regardless of the goodness of the NFW fit.

We find that the concentration derived from the inner parts of the halo is systematically lower than the concentration derived from the halo as a whole at late times, although at early times, the inner concentration is sometimes higher for $\tau \ll t_{\rm dyn}$ or $\tau \gg t_{\rm H}$. However, if the maximum radius used in the fit is $\sim 0.1R_{\rm vir}$, the concentration from the NFW fit is always lower than the concentra-

tion from the NFW fit to the halo as a whole. In general, the discrepancy among concentrations becomes less severe as a larger fraction of the halo particles are used for the fit. The NFW fit becomes better and concentrations tend to be slightly higher if the minimum radius is raised to 10 kpc from 4 kpc, and in general, NFW fits become better as the maximum radius considered in the fit decreases. Fits to the outer part of the halo show a trend that the halo concentration is initially higher than that estimated from the halo as a whole, then dips low, and then becomes relatively high again. This phenomenon is due to the finite time it takes for particles ejected from the inner halo to reach the outer halo, and the longer dynamical (and hence, equilibration) time in the outer halo. The NFW profile is almost always a reasonable fit to the data with $r > 0.5R_{\rm vir}$.

Are these trends consistent with observations? The relatively low concentration measured in the innermost part of the halo relative to the halo as a whole is qualitatively consistent with the low concentrations inferred from low-surface-brightness and dwarf-galaxy rotation curves. However, in the absence of selection biases, one would expect the weak-lensing-derived concentrations to be slightly higher than strong-lensing-derived concentrations for the same halos, and also slightly higher than concentrations inferred from x-ray gas profiles, which is the opposite of what is observed. X-ray and strong-lensing halo samples are likely highly biased towards higher concentrations, and so a better understanding of selection effects is necessary in order to understand the differences in inferred concentration among the various lensing, x-ray, and dynamical probes of dark-matter density profiles.

Nonetheless, the prediction from decaying-dark-matter models is that it is possible that different probes of dark-matter halo profiles will indicate different concentrations for the same halo, even if the NFW profile is shown to be a good fit to data from probes sensitive to the innermost or outermost parts of the halo, such as weak lensing or rotation curves.

V. CONCLUSION

In this work, we have used simulations of two-body dark-matter decay in isolated halos initially in equilibrium to characterize the response of halos as a function of the center-of-mass kick speed v_k, the decay time τ, and time. We find that for the union of the parameter space $v_k/v_{\rm vir} \lesssim 0.2$ and $\tau/t_{\rm dyn} \gtrsim 100$, dark-matter halos are essentially unchanged; the mass loss is $\lesssim 10\%$ over a Hubble time, and the shape of the density profile does not change, although the concentration declines somewhat for $v_k/v_{\rm vir} > 1$. For the union of $v_k/v_{\rm vir} \gtrsim 1$ and $\tau/t_{\rm dyn} \lesssim 10$, there is severe mass loss and a radical change to the shape of the dark-matter density profile. For the rest of the decaying-dark-matter parameter space, there is moderate mass loss and significant deviations of the shape of the

dark-matter density profile relative to the initial halo properties.

We used our simulations in conjunction with the observed mass-concentration relation and the galaxy-cluster mass function to constrain the two-parameter decay parameter space. We find that the mass-concentration relation yields the stronger constraint on τ for a broad range of v_k, constraining $\tau \gtrsim 30$–40 Gyr for $v_k \gtrsim 200 \text{ km s}^{-1}$. Constraints on the decay parameters should improve greatly in the next 5–10 years with blossoming wide-field

Sunyaev-Zel'dovich and optical surveys, and with cosmological simulations of decaying dark matter.

ACKNOWLEDGMENTS

[1] R. Kessler, A. C. Becker, D. Cinabro, J. Vanderplas, J. A. Frieman, J. Marriner, T. M. Davis, B. Dilday, J. Holtzman, and S. W. Jha et al., Astrophys. J. Suppl. Ser. **185,** 32 (2009).

[2] B. A. Reid et al., arXiv:0907.1659.

[3] A. Vikhlinin, A. V. Kravtsov, R. A. Burenin, H. Ebeling, W. R. Forman, A. Hornstrup, C. Jones, S. S. Murray, D. Nagai, and H. Quintana et al., Astrophys. J. **692,** 1060 (2009).

[4] E. Komatsu, K. M. Smith, J. Dunkley, C. L. Bennett, B. Gold, G. Hinshaw, N. Jarosik, D. Larson, M. R. Nolta, and L. Page et al., arXiv:1001.4538.

[5] E. Rozo, R. H. Wechsler, E. S. Rykoff, J. T. Annis, M. R. Becker, A. E. Evrard, J. A. Frieman, S. M. Hansen, J. Hao, and D. E. Johnston et al., Astrophys. J. **708,** 645 (2010).

[6] G. Jungman, M. Kamionkowski, and K. Griest, Phys. Rep. **267,** 195 (1996).

[7] T. Appelquist, H.-C. Cheng, and B. A. Dobrescu, Phys. Rev. D **64,** 035002 (2001).

[8] H.-C. Cheng, J. L. Feng, and K. T. Matchev, Phys. Rev. Lett. **89,** 211301 (2002).

[9] G. Servant and T. M. P. Tait, New J. Phys. **4,** 99 (2002).

[10] J. Hubisz and P. Meade, Phys. Rev. D **71,** 035016 (2005).

[11] B. Moore, S. Ghigna, F. Governato, G. Lake, T. Quinn, J. Stadel, and P. Tozzi, Astrophys. J. **524,** L19 (1999).

[12] S. Davidson, S. Hannestad, and G. Raffelt, J. High Energy Phys. 05 (2000) 003.

[13] K. Sigurdson, M. Doran, A. Kurylov, R. R. Caldwell, and M. Kamionkowski, Phys. Rev. D **70,** 083501 (2004).

[14] D. N. Spergel and P. J. Steinhardt, Phys. Rev. Lett. **84,** 3760 (2000).

[15] S. S. Gubser and P. J. E. Peebles, Phys. Rev. D **70,** 123510 (2004).

[16] M. Kesden and M. Kamionkowski, Phys. Rev. D **74,** 083007 (2006).

[17] M. Kesden and M. Kamionkowski, Phys. Rev. Lett. **97,** 131303 (2006).

[18] L. Ackerman, M. R. Buckley, S. M. Carroll, and M. Kamionkowski, Phys. Rev. D **79,** 023519 (2009).

[19] J. L. Feng, M. Kaplinghat, H. Tu, and H.-B. Yu, J. Cosmol. Astropart. Phys. 07 (2009) 004.

[20] G. D'Amico, M. Kamionkowski, and K. Sigurdson, arXiv:0907.1912.

[21] J. L. Feng, arXiv:1002.3828.

[22] D. Tucker-Smith and N. Weiner, Phys. Rev. D **64,** 043502 (2001).

[23] F. J. Sánchez-Salcedo, Astrophys. J. **591,** L107 (2003).

[24] M. Abdelqader and F. Melia, Mon. Not. R. Astron. Soc. **388,** 1869 (2008).

[25] A. H. G. Peter, Phys. Rev. D **81,** 083511 (2010).

[26] R. A. Flores, G. R. Blumenthal, A. Dekel, and J. R. Primack, Nature (London) **323,** 781 (1986).

[27] R. Cen, Astrophys. J. **546,** L77 (2001).

[28] V. Springel, N. Yoshida, and S. D. M. White, New Astron. Rev. **6,** 79 (2001).

[29] V. Springel, Mon. Not. R. Astron. Soc. **364,** 1105 (2005).

[30] J. F. Navarro, C. S. Frenk, and S. D. M. White, Astrophys. J. **462,** 563 (1996).

[31] J. F. Navarro, C. S. Frenk, and S. D. M. White, Astrophys. J. **490,** 493 (1997).

[32] G. L. Bryan and M. L. Norman, Astrophys. J. **495,** 80 (1998).

[33] J. Diemand and B. Moore, arXiv:0906.4340.

[34] S. Kazantzidis, J. Magorrian, and B. Moore, Astrophys. J. **601,** 37 (2004).

[35] W. H. Press et al., Numerical Recipes in C: The Art of Scientific Computing (University Press, Cambridge, England, 1992), 2nd ed.

[36] C. Power, J. F. Navarro, A. Jenkins, C. S. Frenk, S. D. M. White, V. Springel, J. Stadel, and T. Quinn, Mon. Not. R. Astron. Soc. **338,** 14 (2003).

[37] Y. Lu, H. J. Mo, N. Katz, and M. D. Weinberg, Mon. Not. R. Astron. Soc. **368,** 1931 (2006).

[38] J. S. Bullock, T. S. Kolatt, Y. Sigad, R. S. Somerville, A. V. Kravtsov, A. A. Klypin, J. R. Primack, and A. Dekel, Mon. Not. R. Astron. Soc. **321,** 559 (2001).

[39] A. F. Neto, L. Gao, P. Bett, S. Cole, J. F. Navarro, C. S. Frenk, S. D. M. White, V. Springel, and A. Jenkins, Mon. Not. R. Astron. Soc. **381,** 1450 (2007).

[40] A. V. Macciò, A. A. Dutton, F. C. van den Bosch, B. Moore, D. Potter, and J. Stadel, Mon. Not. R. Astron. Soc. **378,** 55 (2007).

[41] A. R. Duffy, J. Schaye, S. T. Kay, and C. Dalla Vecchia, Mon. Not. R. Astron. Soc. **390,** L64 (2008).

[42] A. V. Macciò, A. A. Dutton, and F. C. van den Bosch, Mon. Not. R. Astron. Soc. **391,** 1940 (2008).

[43] D. H. Zhao, Y. P. Jing, H. J. Mo, and G. Börner, Astrophys. J. **707,** 354 (2009).

[44] D. Larson, J. Dunkley, G. Hinshaw, E. Komatsu, M. R. Nolta, C. L. Bennett, B. Gold, M. Halpern, R. S. Hill, and N. Jarosik *et al.*, arXiv:1001.4635.

[45] D. N. Spergel, L. Verde, H. V. Peiris, E. Komatsu, M. R. Nolta, C. L. Bennett, M. Halpern, G. Hinshaw, N. Jarosik, and A. Kogut *et al.*, Astrophys. J. Suppl. Ser. **148,** 175 (2003).

[46] D. N. Spergel *et al.*, Astrophys. J. Suppl. Ser. **170,** 377 (2007).

[47] J. M. Comerford and P. Natarajan, Mon. Not. R. Astron. Soc. **379,** 190 (2007).

[48] D. A. Buote, F. Gastaldello, P. J. Humphrey, L. Zappacosta, J. S. Bullock, F. Brighenti, and W. G. Mathews, Astrophys. J. **664,** 123 (2007).

[49] R. Mandelbaum, U. Seljak, and C. M. Hirata, J. Cosmol. Astropart. Phys. 08 (2008) 006.

[50] J. F. Hennawi, N. Dalal, P. Bode, and J. P. Ostriker, Astrophys. J. **654,** 714 (2007).

[51] D. H. Rudd, A. R. Zentner, and A. V. Kravtsov, Astrophys. J. **672,** 19 (2008).

[52] J. Annis, S. Bridle, F. J. Castander, A. E. Evrard, P. Fosalba, J. A. Frieman, E. Gaztanaga, B. Jain, A. V. Kravtsov, and O. Lahav *et al.*, arXiv:astro-ph/0510195.

[53] N. Kaiser, H. Aussel, B. E. Burke, H. Boesgaard, K. Chambers, M. R. Chun, J. N. Heasley, K. Hodapp, B. Hunt, and R. Jedicke *et al.*, in *Survey and Other Telescope Technologies and Discoveries*, edited by J. A. Tyson and S. Wolff, SPIE Proceedings Vol. 4836 (SPIE-International Society for Optical Engineering, Bellingham, WA, 2002), pp. 154–164.

[54] P. A. Abell, J. Allison, S. F. Anderson, J. R. Andrew, J. R. P. Angel, L. Armus, D. Arnett, S. J. Asztalos, T. S. Axelrod, and S. Bailey *et al.* (LSST Science Collaborations), arXiv:0912.0201.

[55] P. Predehl, G. Hasinger, H. Böhringer, U. Briel, H. Brunner, E. Churazov, M. Freyberg, P. Friedrich, E. Kendziorra, and D. Lutz *et al.*, in *Space Telescopes and Instrumentation II: Ultraviolet to Gamma Ray*, SPIE Proceedings Vol. 6266 (SPIE-International Society for Optical Engineering, Bellingham, WA, 2006).

[56] A. Albrecht, G. Bernstein, R. Cahn, W. L. Freedman, J. Hewitt, W. Hu, J. Huth, M. Kamionkowski, E. W. Kolb, and L. Knox *et al.*, arXiv:astro-ph/0609591.

[57] E. Romano-Díaz, I. Shlosman, Y. Hoffman, and C. Heller, Astrophys. J. **685,** L105 (2008).

[58] S. Pedrosa, P. B. Tissera, and C. Scannapieco, Mon. Not. R. Astron. Soc. **402,** 776 (2010).

[59] P. B. Tissera, S. D. M. White, S. Pedrosa, and C. Scannapieco, arXiv:0911.2316.

[60] F. Governato, C. Brook, L. Mayer, A. Brooks, G. Rhee, J. Wadsley, P. Jonsson, B. Willman, G. Stinson, and T. Quinn *et al.*, Nature (London) **463,** 203 (2010).

[61] A. R. Duffy, J. Schaye, S. T. Kay, C. Dalla Vecchia, R. A. Battye, and C. M. Booth, arXiv:1001.3447.

[62] W. H. Press and P. Schechter, Astrophys. J. **187,** 425 (1974).

[63] J. R. Bond, S. Cole, G. Efstathiou, and N. Kaiser, Astrophys. J. **379,** 440 (1991).

[64] S. D. M. White, G. Efstathiou, and C. S. Frenk, Mon. Not. R. Astron. Soc. **262,** 1023 (1993).

[65] R. K. Sheth and G. Tormen, Mon. Not. R. Astron. Soc. **329,** 61 (2002).

[66] B. E. Robertson, A. V. Kravtsov, J. Tinker, and A. R. Zentner, Astrophys. J. **696,** 636 (2009).

[67] M. Oguri, K. Takahashi, H. Ohno, and K. Kotake, Astrophys. J. **597,** 645 (2003).

[68] A. Mantz, S. W. Allen, H. Ebeling, and D. Rapetti, Mon. Not. R. Astron. Soc. **387,** 1179 (2008).

[69] J. Dunkley, E. Komatsu, M. R. Nolta, D. N. Spergel, D. Larson, G. Hinshaw, L. Page, C. L. Bennett, B. Gold, and N. Jarosik *et al.*, Astrophys. J. Suppl. Ser. **180,** 306 (2009).

[70] J. P. Henry, A. E. Evrard, H. Hoekstra, A. Babul, and A. Mahdavi, Astrophys. J. **691,** 1307 (2009).

[71] A. Mantz, S. W. Allen, D. Rapetti, and H. Ebeling, arXiv:0909.3098.

[72] J. Tinker, A. V. Kravtsov, A. Klypin, K. Abazajian, M. Warren, G. Yepes, S. Gottlöber, and D. E. Holz, Astrophys. J. **688,** 709 (2008).

[73] J. E. Carlstrom, G. P. Holder, and E. D. Reese, Annu. Rev. Astron. Astrophys. **40,** 643 (2002).

[74] A. D. Hincks, V. Acquaviva, P. Ade, P. Aguirre, M. Amiri, J. W. Appel, L. F. Barrientos, E. S. Battistelli, J. R. Bond, and B. Brown *et al.*, arXiv:0907.0461.

[75] Z. Staniszewski, P. A. R. Ade, K. A. Aird, B. A. Benson, L. E. Bleem, J. E. Carlstrom, C. L. Chang, H. Cho, T. M. Crawford, and A. T. Crites *et al.*, Astrophys. J. **701,** 32 (2009).

[76] K. Ichiki, M. Oguri, and K. Takahashi, Phys. Rev. Lett. **93,** 071302 (2004).

[77] I. Zehavi *et al.*, Astrophys. J. **630,** 1 (2005).

[78] L. E. Strigari, J. S. Bullock, M. Kaplinghat, J. D. Simon, M. Geha, B. Willman, and M. G. Walker, Nature (London) **454,** 1096 (2008).

[79] S. Vegetti, L. V. E. Koopmans, A. Bolton, T. Treu, and R. Gavazzi, arXiv:0910.0760.

[80] L. V. E. Koopmans, M. Barnabe, A. Bolton, M. Bradac, L. Ciotti, A. Congdon, O. Czoske, S. Dye, A. Dutton, and A. Elliasdottir *et al.*, arXiv:0902.3186.

[81] P. J. Marshall, M. Auger, J. G. Bartlett, M. Bradac, A. Cooray, N. Dalal, G. Dobler, C. D. Fassnacht, B. Jain, C. R. Keeton *et al.*, arXiv:0902.2963.

[82] L. A. Moustakas, K. Abazajian, A. Benson, A. S. Bolton, J. S. Bullock, J. Chen, E. Cheng, D. Coe, A. B. Congdon, and N. Dalal *et al.*, arXiv:0902.3219.

[83] U. Seljak, Mon. Not. R. Astron. Soc. **318,** 203 (2000).

[84] Z. Zheng, J. L. Tinker, D. H. Weinberg, and A. A. Berlind, Astrophys. J. **575,** 617 (2002).

[85] K. Abazajian, Z. Zheng, I. Zehavi, D. H. Weinberg, J. A. Frieman, A. A. Berlind, M. R. Blanton, N. A. Bahcall, J. Brinkmann, and D. P. Schneider *et al.*, Astrophys. J. **625,** 613 (2005).

[86] Z. Zheng, A. A. Berlind, D. H. Weinberg, A. J. Benson, C. M. Baugh, S. Cole, R. Davé, C. S. Frenk, N. Katz, and C. G. Lacey, Astrophys. J. **633,** 791 (2005).

[87] Z. Zheng and D. H. Weinberg, Astrophys. J. **659,** 1 (2007).

[88] G. Gilmore, M. I. Wilkinson, R. F. G. Wyse, J. T. Kleyna, A. Koch, N. W. Evans, and E. K. Grebel, Astrophys. J. **663,** 948 (2007).

[89] L. E. Strigari, J. S. Bullock, and M. Kaplinghat, Astrophys. J. **657,** L1 (2007).

[90] L. E. Strigari, S. M. Koushiappas, J. S. Bullock, M. Kaplinghat, J. D. Simon, M. Geha, and B. Willman, Astrophys. J. **678**, 614 (2008).

[91] M. G. Walker, M. Mateo, E. W. Olszewski, J. Peñarrubia, N. Wyn Evans, and G. Gilmore, Astrophys. J. **704**, 1274 (2009).

[92] E. J. Tollerud, J. S. Bullock, L. E. Strigari, and B. Willman, Astrophys. J. **688**, 277 (2008).

[93] M. I. Wilkinson and N. W. Evans, Mon. Not. R. Astron. Soc. **310**, 645 (1999).

[94] J. D. Simon, A. D. Bolatto, A. Leroy, L. Blitz, and E. L. Gates, Astrophys. J. **621**, 757 (2005).

[95] W. J. G. de Blok, F. Walter, E. Brinks, C. Trachternach, S.-H. Oh, and R. C. Kennicutt, Astron. J. **136**, 2648 (2008).

[96] R. Kuzio de Naray, S. S. McGaugh, and W. J. G. de Blok, Astrophys. J. **676**, 920 (2008).

[97] L. V. E. Koopmans, T. Treu, A. S. Bolton, S. Burles, and L. A. Moustakas, Astrophys. J. **649**, 599 (2006).

[98] A. B. Newman, T. Treu, R. S. Ellis, D. J. Sand, J. Richard, P. J. Marshall, P. Capak, and S. Miyazaki, Astrophys. J. **706**, 1078 (2009).

[99] J. Richard, G. P. Smith, J. Kneib, R. Ellis, A. J. R. Sanderson, L. Pei, T. Targett, D. Sand, M. Swinbank, and H. Dannerbauer *et al.*, arXiv:0911.3302.

[100] R. Mandelbaum, U. Seljak, R. J. Cool, M. Blanton, C. M. Hirata, and J. Brinkmann, Mon. Not. R. Astron. Soc. **372**, 758 (2006).

[101] P. J. Humphrey, D. A. Buote, F. Gastaldello, L. Zappacosta, J. S. Bullock, F. Brighenti, and W. G. Mathews, Astrophys. J. **646**, 899 (2006).

[102] F. Gastaldello, D. A. Buote, P. J. Humphrey, L. Zappacosta, J. S. Bullock, F. Brighenti, and W. G. Mathews, Astrophys. J. **669**, 158 (2007).

[103] R. Mandelbaum, G. van de Ven, and C. R. Keeton, Mon. Not. R. Astron. Soc. **398**, 635 (2009).

[104] J. M. Comerford, M. Meneghetti, M. Bartelmann, and M. Schirmer, Astrophys. J. **642**, 39 (2006).